Science Advances
AAAS

advances.sciencemag.org/cgi/content/full/6/25/eaba7678/DC1

# Supplementary Materials for

## *Operando* detection of single nanoparticle activity dynamics inside a model pore catalyst material

David Albinsson, Stephan Bartling, Sara Nilsson, Henrik Ström, Joachim Fritzsche, Christoph Langhammer*

*Corresponding author. Email: clangham@chalmers.se

Published 19 June 2020, *Sci. Adv.* **6**, eaba7678 (2020)
DOI: 10.1126/sciadv.aba7678

**The PDF file includes:**



**Other Supplementary Material for this manuscript includes the following:**

(available at advances.sciencemag.org/cgi/content/full/6/25/eaba7678/DC1)

# 1 Nanoreactor Platform

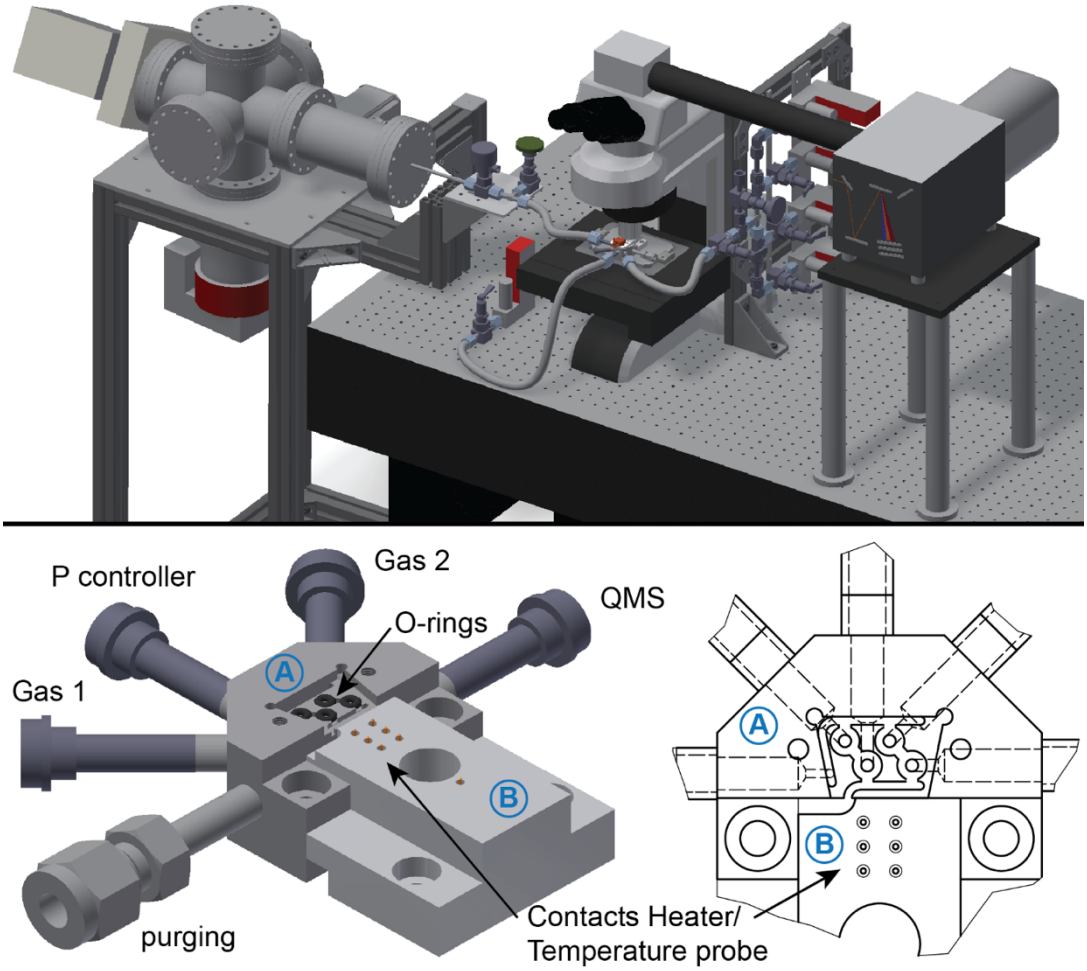


**Fig. S1. Schematic illustration and technical drawing of the complete setup (upper image) and connection block (lower image) that hosts the nanofluidic chip under the microscope.** Part A is manufactured in stainless steel and provides the gas connections to the chip that is pressed against four FPM O-rings. Electrical contacts for resistive heating and a 4-wire RTD sensor are realized with electronic spring pins embedded in part B made out of machined ceramic.

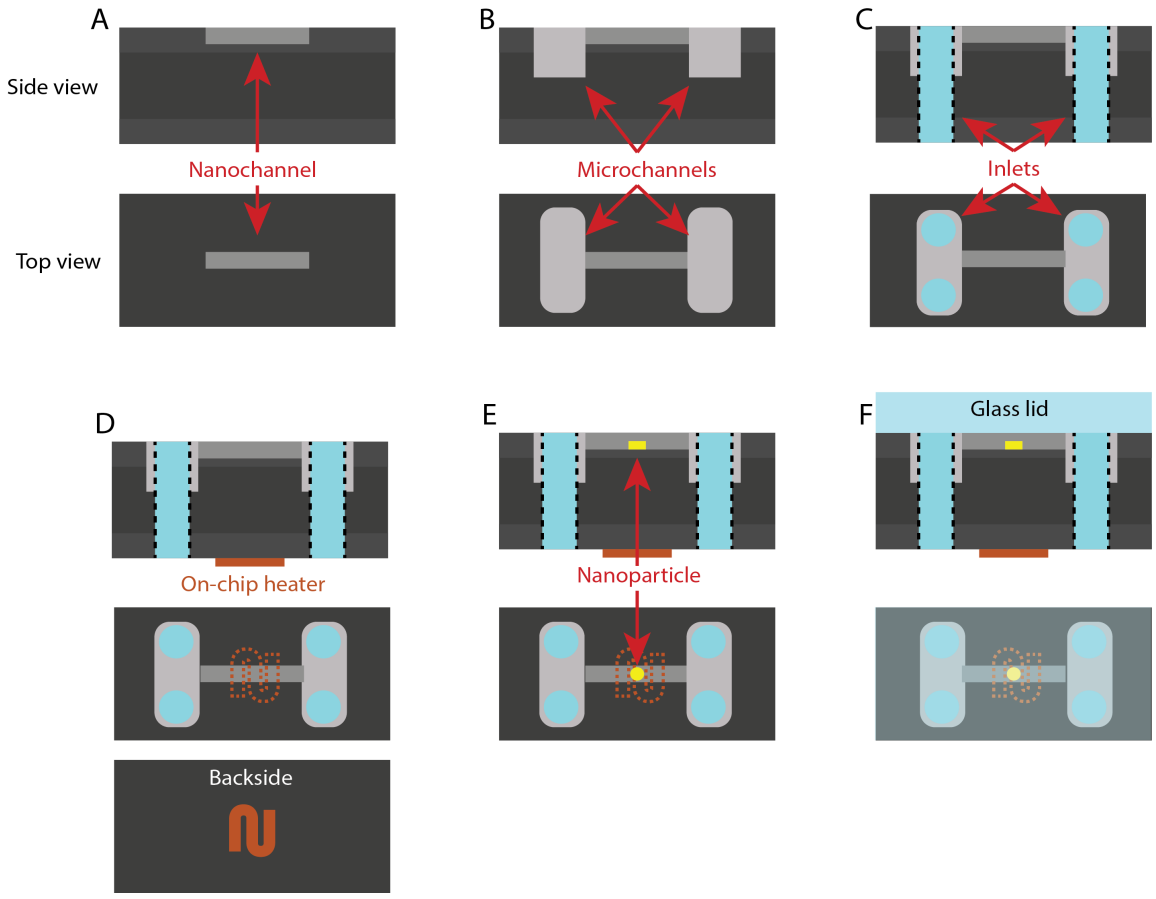


**Fig. S2. Process flow for the nanofabrication of the chip onto a thermally oxidized Si wafer with 200 nm oxide**. A) Nanofluidic model pores are patterned using EBL and etched using RIE to 100 nm depth. B) Microchannels are patterned using photo-lithography and etched using DRIE. C) Holes are patterned using photo-lithography from the backside and etched using DRIE. D) A heater pattern is defined on the backside of the chip using photo-lithography and deposited using electron beam deposition of 10 nm Cr followed by 100 nm Pt. e) Nanoparticles are defined in resist using EBL and deposited using electron beam deposition of the desired material. F) A glass lid is bonded to seal the chip.

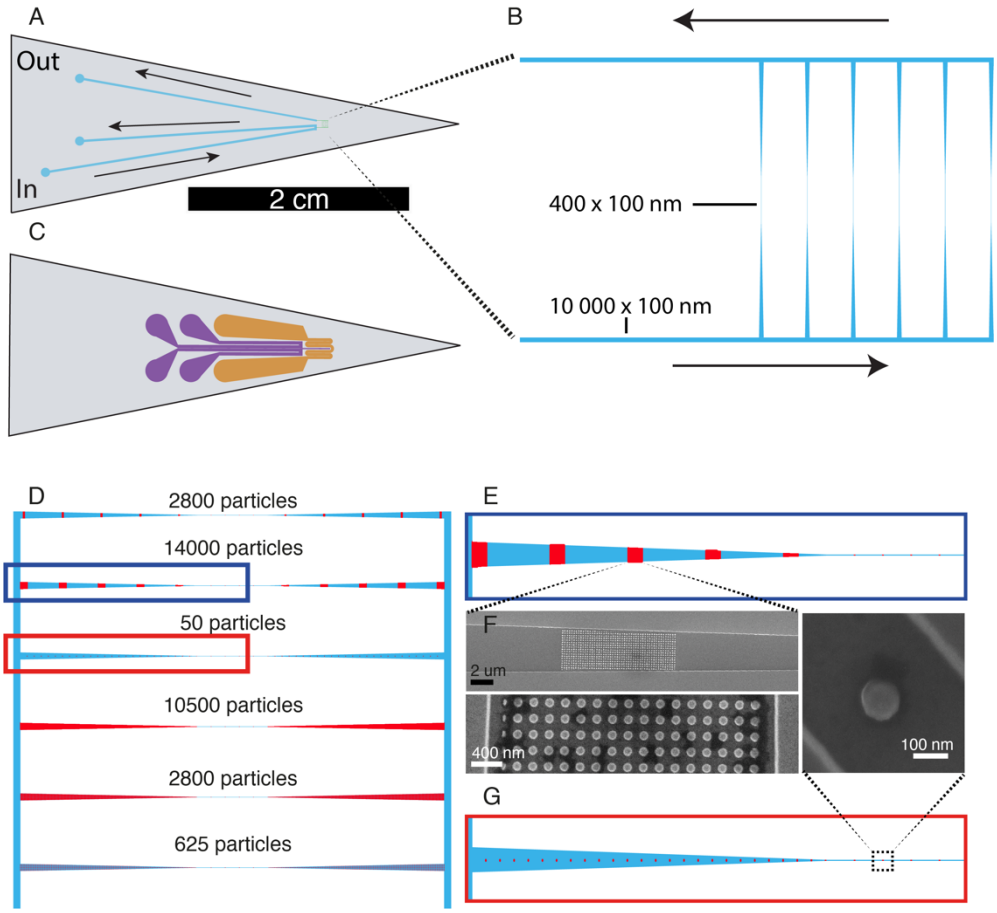


**Fig. S3. Nanofluidic chip design.** A) Drawing of the chip with the microfluidic system shown as blue lines. The cross-sectional dimensions of these microchannels are 60 × 150 µm to allow for fast gas exchange. B) Zoom-in on the nanofluidic system located at the "tip" of the chip and connected to the microfluidic channels. It is comprised of six parallel nanofluidic model pores with cross-sectional dimensions as indicated in the figure. C) Drawing of the backside of the chip with the resistive Pt thin film heater (yellow) and resistance thermometer (purple). D) Overview of the six model pores decorated with different constellations of nanoparticles. E) Zoom-in sketch of a model pore filled with arrays of identical nanoparticles. F) SEM micrographs of a Cu nanoparticle array and of a single Cu nanoparticle placed in narrowest region of the model pore. G) Zoom-in sketch of a model pore filled with a single row of identical particles.

## 2 Experimental system characterization

**Molecular Flow rate**

To characterize the gas flow through the chip and the model pores we have performed several experimental tests and theoretical calculations to reveal the flow- and pressure characteristics. For the experimental flow measurements, the inlet pressure of pure Ar was kept constant. The gas flowing through the chip was then allowed to fill up a closed volume ($4.97 \times 10^{-5}$ m$^3$), connected to the outlet of the chip, that had been evacuated before the experiment. The corresponding pressure rise with time was then monitored using a Pirani gauge. In **Fig. S4** the increasing pressure is plotted as a function of time for three different inlet pressures. Using the ideal gas law the molecular flow into a known volume can be calculated as:

$$\dot{N}(t) = \frac{V}{k_B T} \frac{dp_v(t)}{dt} \qquad (S1)$$

with $\dot{N}(t)$ being the number of gas molecules entering the system per unit time, $p_v(t)$ the pressure in the fixed volume, $V$ the fixed volume, $k_B$ the Boltzmann constant and $T$ the absolute temperature. In addition to the Ar flow through the model pores the leaking trough the O-rings contributes to the measured flow of gas molecules entering the system and corresponds to about $10^5$ molecules/s. The measured flow rates through the model pores span $4 \times 10^{11} - 8 \times 10^{11}$ molecules/s for inlet pressures in the range of 2 – 4 bar.

**Gas residence time in Nanoreactor**

The residence time of reactants inside a model pore was estimated based on the volume of a model pore ($V_{channnel}$) and the volumetric flow rate ($Q_{channel}$) through each pore. Assuming a total pressure of 2 bar and an operation temperature of 500 K, the residence time was calculated as

$$\tau = \frac{V_{channel}}{Q_{channel}},$$

where $V_{channel} = 254\ \mu m^3$ and $Q_{channel}$ was found via the ideal gas law as

$$Q_{channel} = \frac{\dot{n} k_B T}{P} = 3450 \frac{\mu m^3}{s},$$

where $\dot{n} = 1 \times 10^{11}\ s^{-1}$ is the molecular flow rate, $k_B$ is Boltzmann's constant, $P$ = 2 bar is the pressure and $T$ = 500 K is the temperature, leading to $\tau$ = 0.07 s.

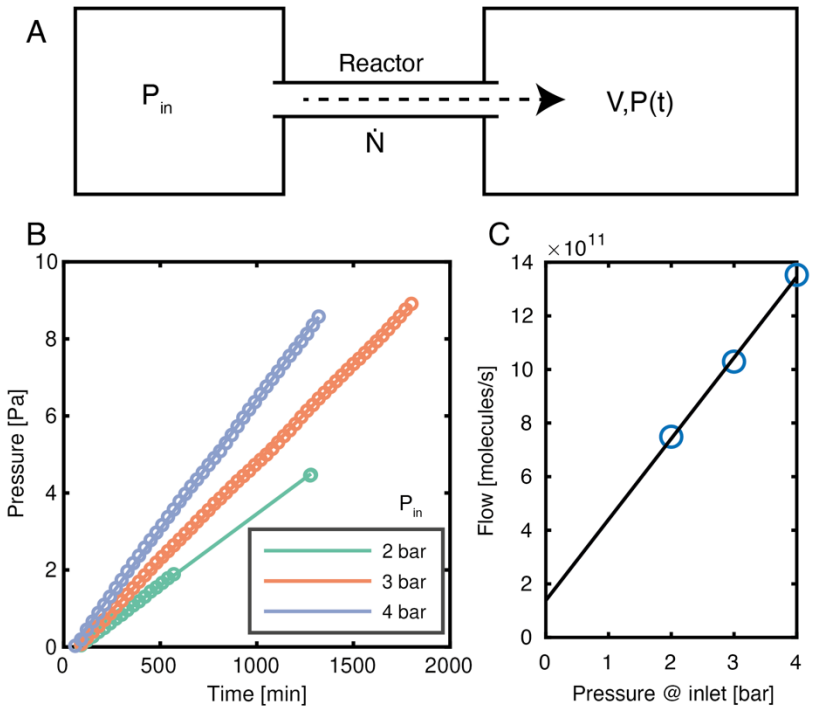


**Fig. S4. Flow through the nanofluidic chip.** A) Schematic depiction of the experimental setup for flow characterization through the nanofluidic chip. A constant pressure, $P_{in}$, is set on the inlet side of the chip while the outlet is connected to a closed known volume, $V$. The pressure in the closed volume is monitored over time and is presented for three different inlet pressures in (B). The slope of the pressure increase can be converted to a molecular flow (eq. S1), which is presented for the three sets of inlet pressures in panel (C).

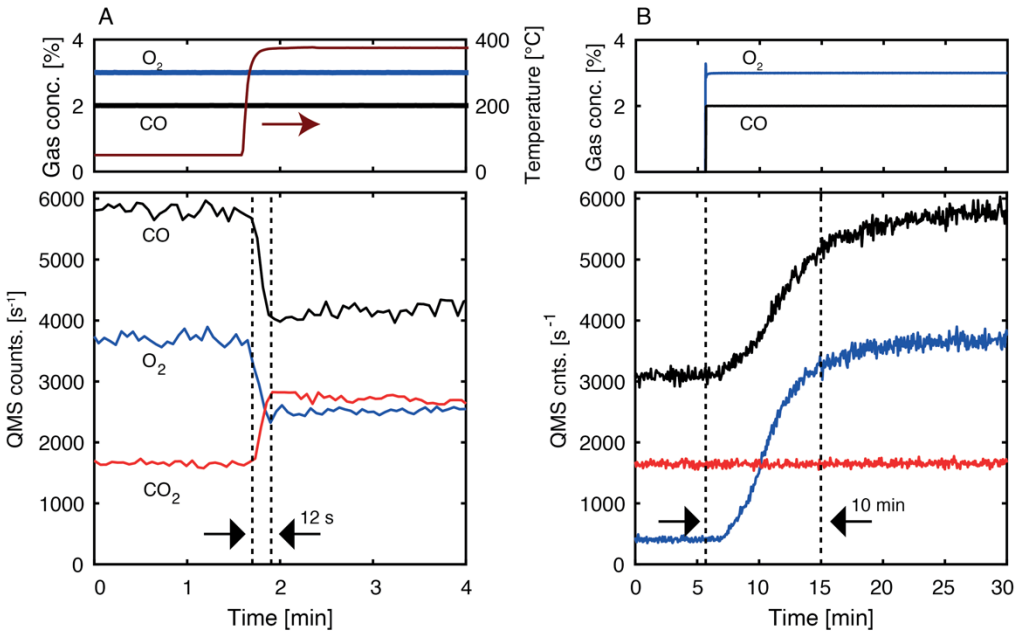


**Fig. S5. Temporal response of a nanoreactor with Au-Pd hybrid nanostructures.** A) The top panel shows the set gas concentration of $O_2$ and CO over time together with the measured chip temperature. A continuous flow of 2% CO and 3% $O_2$ was established through the system. Then, the chip temperature was increased from 323 K to 648 K in approximately 5 seconds. This temperature increase results in a significant increase in the catalytic activity of Pd, resulting in an increased CO oxidation into $CO_2$. The QMS response of CO, $O_2$ and $CO_2$ is presented in the bottom panel. A clear increase in $CO_2$ production is seen within 12 s, together with a corresponding decrease in CO and $O_2$. B) To measure the gas exchange delay and time constant of the setup, a step of CO and $O_2$ was set on the mass flow controller, as shown in the top panel. The corresponding QMS response is presented in the bottom panel, where a ca. 10 min delay is observed.

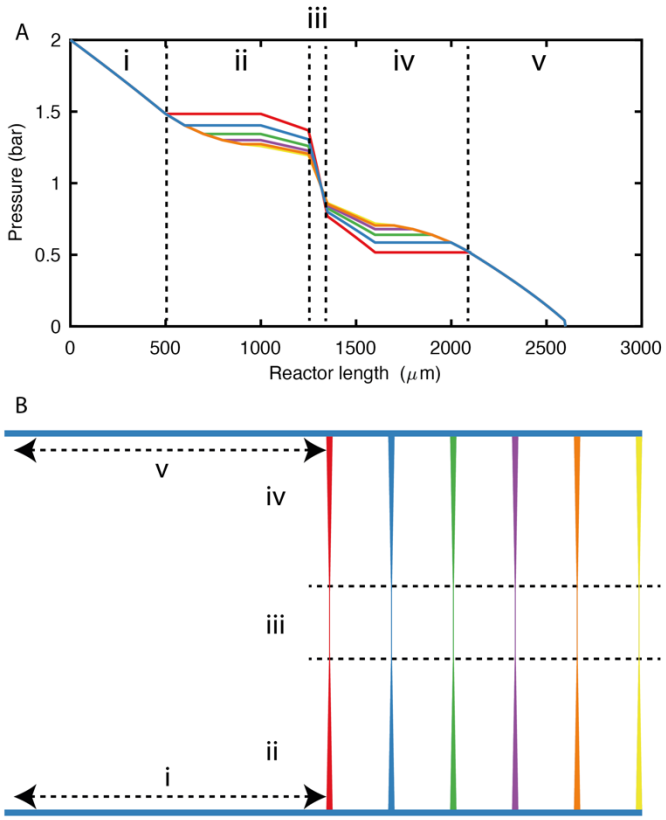


**Fig. S6. Calculated pressure profile.** (A) The pressure profile across the nanofluidic chip calculated using a model for the whole Knudsen regime, presented as a function of fluidic system length The colors correspond to the six parallel model pores illustrated in (B), with its different regions indicated by Roman letters i-v. Due to the different total lengths of the six model pores, flat regions have been added to the pressure profile (top panel) to better be able to compare the pressure profile in the central parts of all model pores. (B) Schematic of the nanofluidic system containing the model pores (colored) with regions marked in Roman letters to indicate the locations also defined in (A).

## 3 Hydrogen sorption by single Pd nanoparticles

By tracking the individual dark field scattering spectra of the strongly scattering Au nanoantenna placed adjacent to a more weakly scattering Pd nanoparticle, changes in the Pd particle can be detected. Specifically changes in permittivity and volume expansion of Pd when undergoing the first order phase transition to the hydride results in a distinct change of the scattering cross-section of the Au-Pd hybrid nanostructure. This hydride formation phase transition occurs readily in Pd at ambient conditions(*44*). During absorption, $H_2$ dissociates on the Pd surface and subsequently occupies surface, subsurface and interstitial lattice sites according to their specific energetics(*45*). In the bulk, at low hydrogen partial pressures, the hydrogen atoms form a solid solution ($\alpha$-phase). Then, at each temperature below the critical temperature, there is a pressure at which the chemical potentials of hydrogen in the gas phase, $\alpha$-phase and hydride ($\beta$-phase) are equal, and the first-order transition to the $\beta$-phase is initiated and manifested as a plateau in a pressure composition isotherm. Depending on the exact relative position of the Au antenna and the Pd particle undergoing a phase transition, the optical response can vary significantly.(*26*) Here, we choose to rely on the change in the full width at half maximum (FWHM) of the scattering peak, in contrast to the more typically used peak position change ($\lambda_P$). This is based on the fact that the FWHM signal is less sensitive to long term drift, as well as gives a larger signal-to-noise ratio compared to the corresponding change in $\lambda_P$ in our system (**Fig. S7** and **Fig. S8** for FWHM and $\lambda_P$ responses, respectively).

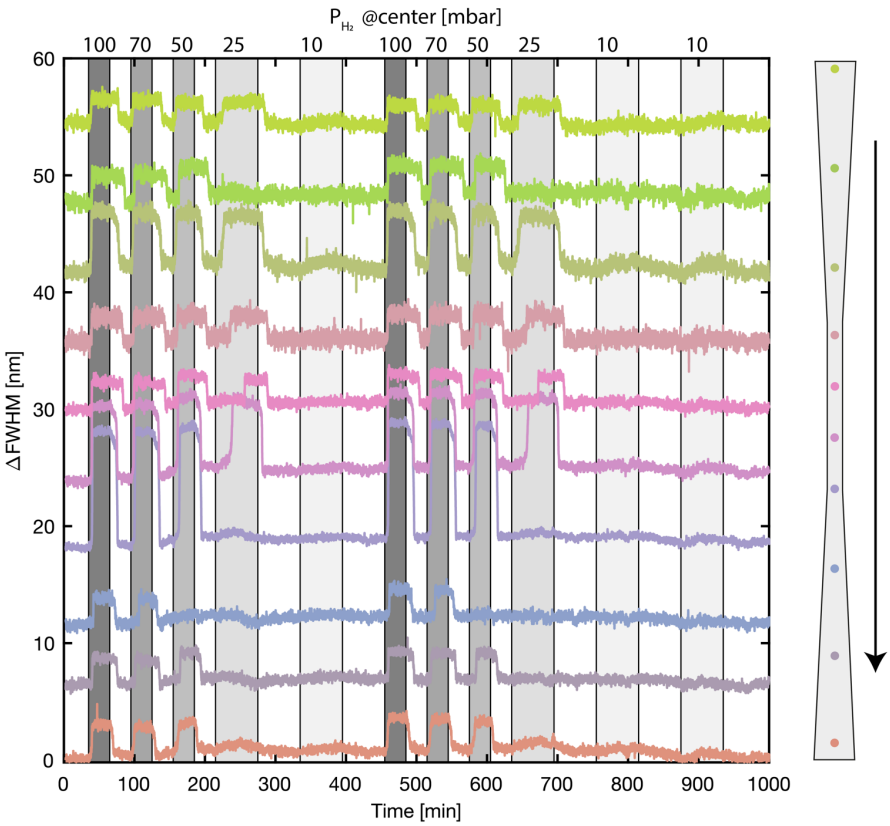


**Fig. S7. Hydride formation in single Pd nanoparticles at different hydrogen partial pressures.** Hydrogen sorption induces a first order phase transformation at a critical hydrogen partial pressure where hydride formation occurs. This transformation then induces a change in optical response of the Pd nanoparticle – here expressed as a change in the full-width-at-half-maximum (FWHM) of its scattering peak. The color code depicts different single nanoparticles placed along the nanofluidic model pore and measured simultaneously, as indicated in the schematic to the right. The arrow indicates flow direction. Pulses of $H_2$ gas supplied at different partial pressures are indicated by the gray shaded areas with the estimated (using the calculations described above) $H_2$ partial pressure at the center of the pore indicated in the top x-axis.

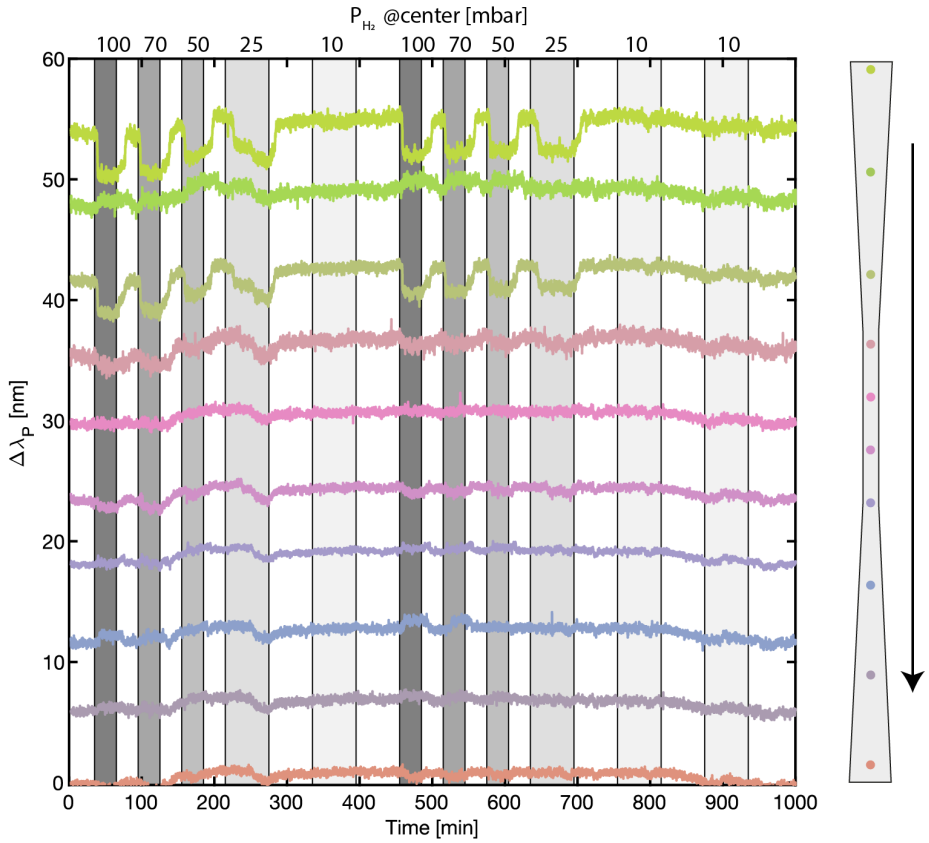


**Fig. S8. Hydride formation in single Pd nanoparticles at different hydrogen partial pressures.** Same as **Fig. S7** but with the single particle optical response expressed as a change in the LSPR peak position ($\lambda_P$) of the individual scattering peaks. The color code depicts different single nanoparticles placed along the nanofluidic model pore, as indicated in the schematic to the right. Pulses of $H_2$ gas supplied at different partial pressures are indicated by the gray shaded areas.

## 4 CO oxidation over Cu

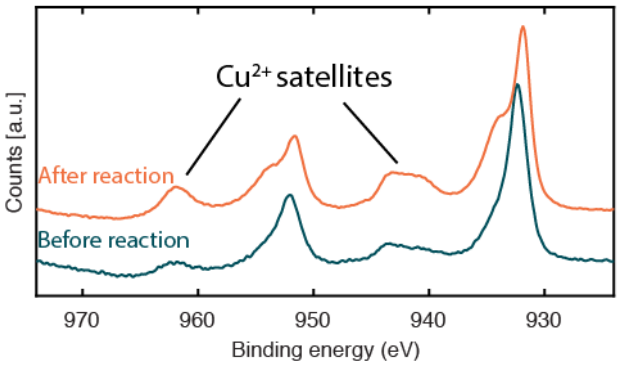


**Fig. S9. XPS measurements of Cu nanoparticles before and after reaction.** Cu nanoparticle sample analogues where fabricated using hole-mask colloidal lithography,(*46*) yielding an array of disk shaped, 100 nm diameter and 40 nm high, Cu particles on an open surface to enable XPS analysis of their oxidation state before and after reaction. The corresponding Cu2p XPS spectra were collected before and after the sample was treated in identical reaction conditions as in the experiment discussed in Fig. 3 in the main text. After exposure to reaction conditions (493 K 6 % CO and 0.5% $O_2$ in Ar) there is a clear appearance of satellite peaks at ca. 942 eV and 962 eV, indicative of the formation of CuO. The shoulder like features on the two main peaks are a result of a mixed oxide, where the peak at the lowest energy corresponds to $Cu_2O$ and the higher energy peak to CuO.

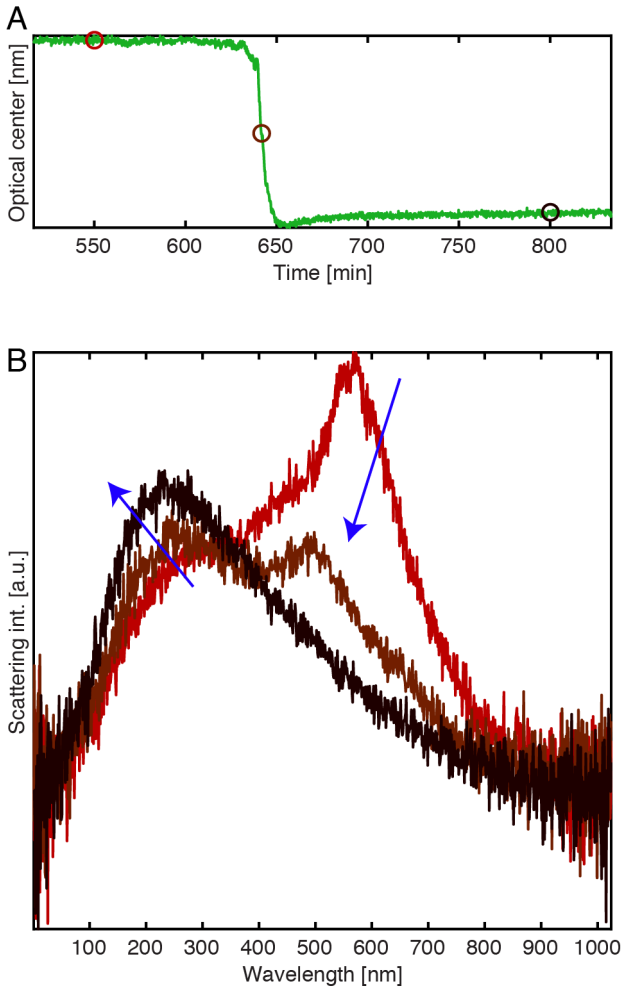


**Fig. S10. Scattering spectra of single Cu nanoparticles during oxidation.** (A) Optical center (defined in eq. S2) of a single particle scattering spectrum as a function of time during an oxidation event. The distinct decrease in the signal indicates oxidation of the particle. The markers (o) correspond to positions of the snapshots presented in (B). (B) Three spectra of a single Cu nanoparticle before, during and after oxidation. Arrows indicate the order of the spectral change from metallic to oxide.

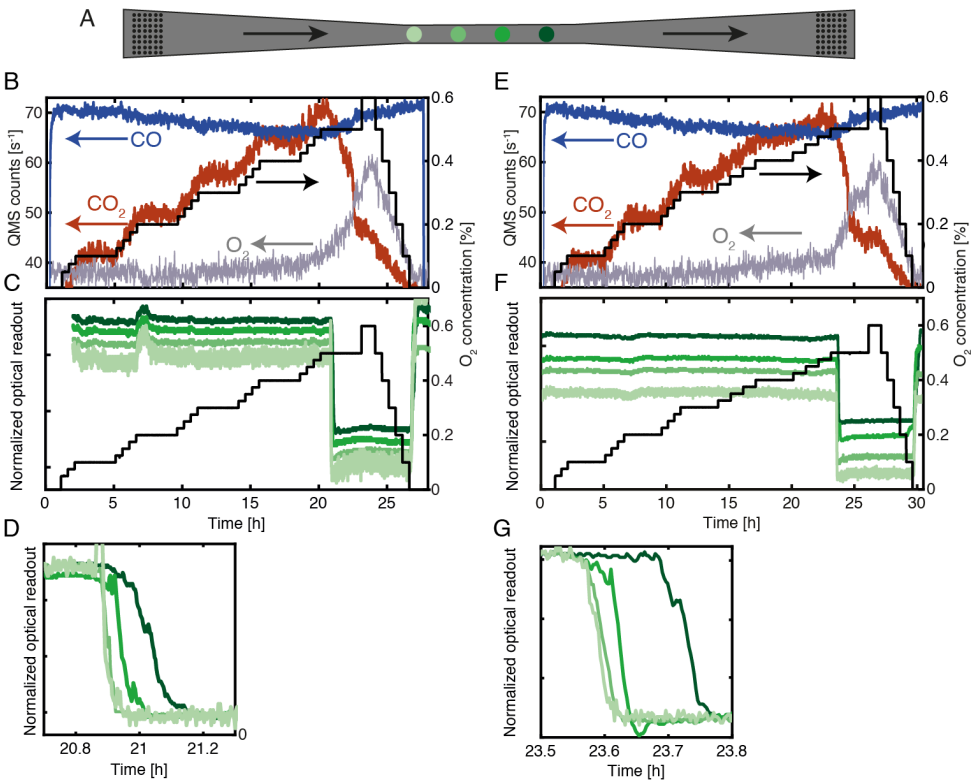


**Fig. S11. Repeated experiments similar to the one presented in Fig. 3 in the main text.** Repeating the experiment depicted in Fig. 3 in the main text results in qualitatively the same trends. Comparing the different experiments reveals that the general trend is reproducible, but the threshold concentration for oxidation, as well as the time delay, is somewhat different for each repetition. We attribute this to irreversible morphological changes of the Cu particles due to repeated oxidation and reduction, as recently reported to result in significant enhancement in catalytic activity(*47*). (A) Schematic of the center part of a nanofluidic model pore (channel 2 in **Fig. 1C**) containing arrays of 100 × 40 nm Cu nanoparticles in the tapered regions and four individual nanoparticles in the narrow center, separated by 20 µm. Note that the size and number of particles are not drawn to scale. Arrows indicate flow direction. (B) Schematic depiction of the set nominal $O_2$ concentration in the system (black) together with the measured QMS response for CO (blue) $O_2$ (gray) and $CO_2$ (red). Note that the CO signal is scaled by a factor 1/8. (C) Optical response of the four single Cu nanoparticles upon increasing $O_2$ concentration during reaction with CO. The black line depicts the set nominal $O_2$ concentration. (D) Zoom-in on the optical center response from panel (C). (E-G) Same as (B-D) for another repeated experiment at the same conditions.

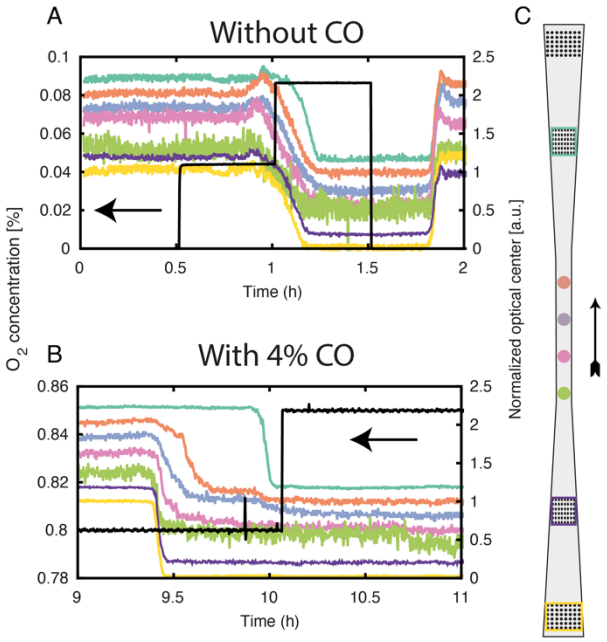


**Fig. S12. Oxidation delay of Cu nanoparticles in the presence and absence of CO.** A) Optical response of four individual Cu nanoparticles and three areas ("patches") containing dense arrays (ca. 200 particles) of identical Cu particles under oxidizing conditions in the absence of CO, as depicted in the schematic in (C). The chip temperature was 493 K. It reveals the simultaneous oxidation of all particles and patches, and that oxidation starts at 0.04 % $O_2$. B) The same particles and patches initially again in the metallic state, now exposed to 4% CO together with 0.8% $O_2$ in the feed, which is needed to induce the Cu oxidation process. In contrast to the CO-free case now there is a delay of ca. 30 minutes between the oxidation of the first and the last patch. C) Schematic of the center part of a model pore corresponding to channel 2 in **Fig. 1C.**

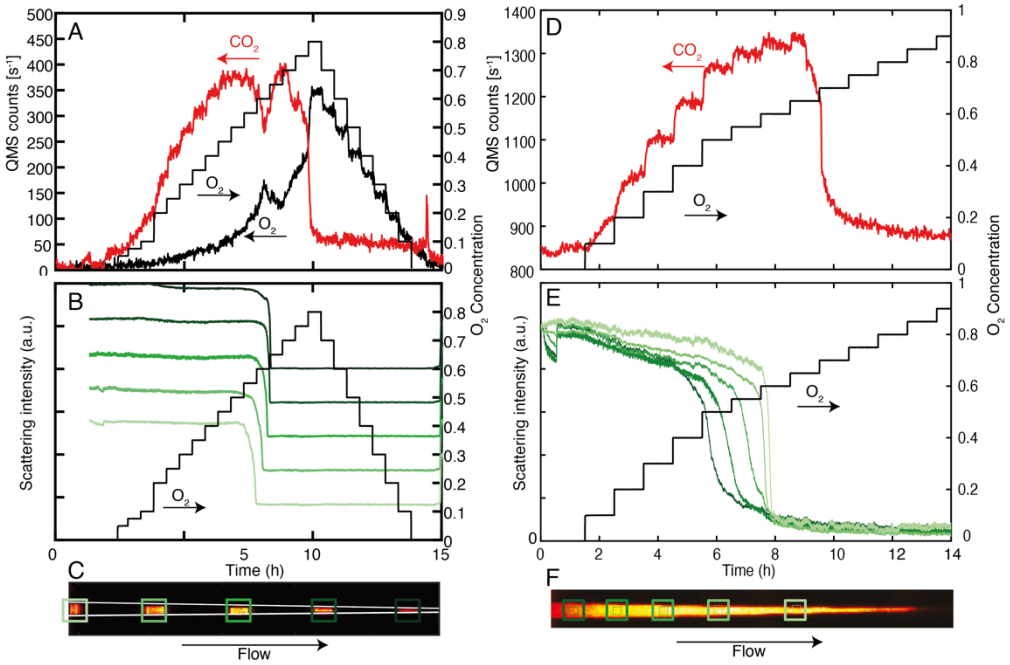


**Fig. S13. CO oxidation over Cu at 498K and 6% CO with optical measurements from different channels.** (A) QMS response for $CO_2$ (red) and $O_2$ (black) together with the corresponding $O_2$ concentration set at the chip inlet (black steps). The observed transient dip in $CO_2$ production after the initial increase is attributed to dynamic changes of catalyst particles outside of the field of view presented in this figure. (B) Scattering intensity of five dense Cu nanoparticle arrays, each containing 300 – 2500 particles (positions in channel are indicated in (C)). (C) Microscope image of the channel (#2 in **Fig. 1C**) with the particle arrays toned in red and green squares to identify the different intensity traces presented in (B). (D) QMS response for $CO_2$ (red) and $O_2$ concentration set at the chip inlet (black steps). (E) Scattering intensity extracted from five locations within the dense array of Cu (the whole array contains ~5000 particles and the positions where the scattering intensity was extracted are indicated in (F)). (F) Microscope image of the channel (#4 in **Fig. 1C**) with the dense particle array toned in red and green squares to identify the position where the local scattering intensities were extracted.

## 5 Optical center definition

The optical center is used to characterize the center of mass of a measured optical spectrum and is defined as:

$$\int_{\lambda_{min}}^{\lambda_{center}} S(\lambda)\, d\lambda = 0.5 \int_{\lambda_{min}}^{\lambda_{max}} S(\lambda)\, d\lambda \qquad (S2)$$

where $\lambda_{center}$ is the optical center, S is the wavelength dependent scattering intensity, and $\lambda_{min}$ and $\lambda_{max}$ are the maximum and minimum wavelength points that were measured, respectively.

## 6 Cu nanoparticle oxidation during CO oxidation

Based on the observed delay in oxidation between individual Cu nanoparticles placed in sequence in a model pore (**Fig. 3** and **Fig. S11**), a theoretical analysis was performed to test the hypothesis that a single Cu nanoparticle can reduce the $O_2$ concentration in the stream enough to inhibit downstream nanoparticle oxidation.

As a first approach, the reduction of $O_2$ in the stream was assumed to occur through reaction with CO on the Cu surface to form $CO_2$. Based on the experimental data presented in **Fig 3B**, we see that an increase from 0.300 % to 0.325 % $O_2$ in the gas feed initiates the oxidation of the Cu nanoparticles. Thus, if the reaction rate from a single particle is high enough to lower the gas stream $O_2$ concentration by 0.025% it is assumed to inhibit oxidation of particles downstream. Based on the flow measurements (**Fig. S4**) the total flow through a single nanofluidic model pore at an inlet pressure of 4 bar is approximately $1.3 \times 10^{11}$ molecules / s. The required $O_2$ consumption via the CO oxidation reaction over a single Cu nanoparticle can be calculated as

$$\dot{N}_{O_2} = c_{O_2} \times \dot{N}_{channel} = 0.00025 \times 1.3 \times 10^{11} \approx 3.3e7\ s^{-1} \qquad (S3)$$

where $c_{O_2}$ is the required concentration drop and $\dot{N}_{channel}$ is the molecular flow through a model pore. By approximating the Cu nanoparticle as a cylindrical structure with a radius of $r_{Cu}$ = 50 nm and a height, $h$ = 40 nm, the exposed surface area is:

$$A_{Cu} = \pi \times r_{Cu}^2 + \pi \times 2\mathrm{r_{Cu}} \times h = \ 2.042\ \times 10^4\ nm^2 \qquad (S4)$$

Assuming an fcc structure with (111) facets exposed, the surface density of atoms in Cu is approximately 14 atoms / nm$^2$. The required turn over frequency (TOF) per exposed surface atom (assumed to be the active site) to reduce the $O_2$ concentration in the flow by 0.025 % is then given by:

$$TOF_{req} = \frac{\dot{N}_{O_2}}{A_{Cu} \times 14} \approx 115\ s^{-1} \qquad (S5)$$

which sets a lower bound for the TOF required to lower the $O_2$ concentration in the stream by 0.025 %. This number can be compared to theoretical TOF's for the CO oxidation reaction on Cu, calculated by DFT, that give values in the range 100 – 1000 s$^{-1}$ at the investigated temperature (*36*).

The second consideration was to investigate the spatial distribution of $O_2$ inside the model pore via finite-volume simulations. The model used is described in the methods section where the parameter $A$ in eq. 1 and 2 was chosen to match the experiment. Physically, $A$ can be translated to a reaction rate over a single nanoparticle that is approximately $5 \times A$ molecules/s (at an inlet mass fraction of 0.001). Setting $A = 10^7$ s$^{-1}$ thus corresponds to a reaction rate that is comparable to the required rates estimated by eq. S3. Varying the value of $A$ in the range $10^5$ s$^{-1}$ to $10^7$ s$^{-1}$ results in qualitatively similar concentration profiles inside the model pore where the magnitude of the concentration drops at each active particle is determined by $A$ (**Fig. S14A**). Additionally, the effect of the total molecular flow rate was investigated by invoking a fully mass-transport limited regime ($A \rightarrow \infty$). The resulting concentration profiles of the tracer, corresponding to $O_2$, for three different molecular flow rates are presented in **Fig. S14B** and reveal that conversion up to 99 % over a single particle is possible at the simulated flowrate close to the one measured for our model pore system (c.f. **Fig. S4C**). The simulations also reveal that at the flow rates relevant to our experiment, the upstream depletion of the reactants due to mass-transfer limited reaction on a downstream (unoxidized and thus highly active)

particle can be significant enough to have a sizable impact on the local reactant (and thus $O_2$) concentration experienced by the closest upstream particle. This effect could thus be an additional contributing factor to the observed significant delay times between single particle oxidation in the model pore.

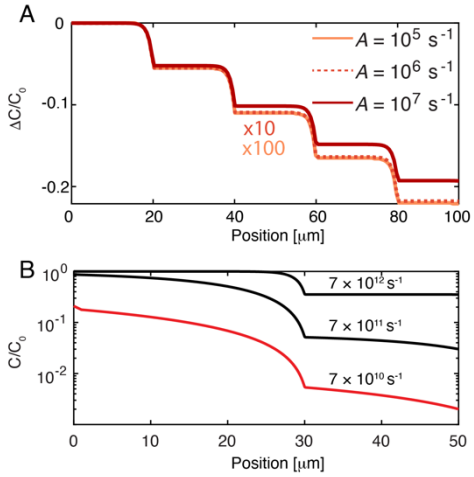


**Fig. S14. Simulated $O_2$ consumption in a nanofluidic model pore.** (a) Relative change of the concentration profile along the flow direction of a model pore at a flowrate of $9 \times 10^{11}$ molecules/s with values for the reaction parameter $A$ (that is used to calculate $R$ in eq. 1 in the materials & methods section) indicated in the legend. Note that the lines are scaled by different factors as indicated in the figure to be able to highlight the similar shape of the profiles. $C_0$ corresponds to the tracer concentration at the inlet of the model pore. (b) Relative concentration profile of a tracer species that is consumed upon interaction with a nanoparticle located at the 30 μm position inside a model pore in the mass-transport limited regime ($A \rightarrow \infty$). The simulations were done for the three different molecular flow rates indicated in the figure. $C_0$ corresponds to the original tracer concentration fed into the model pore.

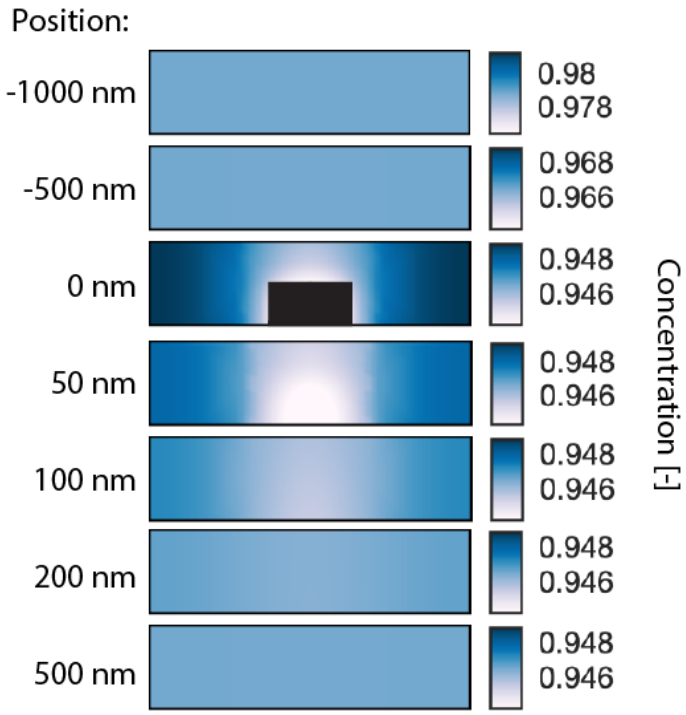


**Fig. S15. 2D contour plots of simulated reactant concentration for model pore cross-sections taken at different positions along the pore.** This is a wider dataset but otherwise identical to what is presented in Fig. 5C. The positions indicated to the left are taken relative to the nanoparticle center. Thus, 0 nm is right at the center of the particle and 50 nm is just after the particle. Scale bars are different for each panel, but share the same range to illustrate the even concentration profile before and after the active particle. Note how diffusion quickly eliminates reactant gradients in the model pore cross-sectional direction.

**Movie S1.**

Optical response from patches containing Cu nanoparticles as they sequentially oxidize under increasing $O_2$ partial pressure. The Movie corresponds to the data presented in **Fig. S13A.**

## REFERENCES AND NOTES


1. J. B. Sambur, P. Chen, Approaches to single-nanoparticle catalysis. *Annu. Rev. Phys. Chem.* **65**, 395–422 (2014).
2. X. Zhou, N. M. Andoy, G. Liu, E. Choudhary, K.-S. Han, H. Shen, P. Chen, Quantitative super-resolution imaging uncovers reactivity patterns on single nanocatalysts. *Nat. Nanotechnol.* **7**, 237–241 (2012).
3. I. L. C. Buurmans, B. M. Weckhuysen, Heterogeneities of individual catalyst particles in space and time as monitored by spectroscopy. *Nat. Chem.* **4**, 873–886 (2012).
4. S. B. Vendelbo, C. F. Elkjær, H. Falsig, I. Puspitasari, P. Dona, L. Mele, B. Morana, B. J. Nelissen, R. van Rijn, J. F. Creemer, P. J. Kooyman, S. Helveg, Visualization of oscillatory behaviour of Pt nanoparticles catalysing CO oxidation. *Nat. Mater.* **13**, 884–890 (2014).
5. W. Wang, Imaging the chemical activity of single nanoparticles with optical microscopy. *Chem. Soc. Rev.* **47**, 2485–2508 (2018).
6. E. M. van Schrojenstein Lantman, T. Deckert-Gaudig, A. J. G. Mank, V. Deckert, B. M. Weckhuysen, Catalytic processes monitored at the nanoscale with tip-enhanced Raman spectroscopy. *Nat. Nanotechnol.* **7**, 583–586 (2012).
7. W. Karim, C. Spreafico, A. Kleibert, J. Gobrecht, J. VandeVondele, Y. Ekinci, J. van Bokhoven, Catalyst support effects on hydrogen spillover. *Nature* **541**, 68–71 (2017).
8. F. Meirer, B. M. Weckhuysen, Spatial and temporal exploration of heterogeneous catalysts with synchrotron radiation. *Nat. Rev. Mater.* **3**, 324–340 (2018).
9. T. Hartman, R. G. Geitenbeek, G. T. Whiting, B. M. Weckhuysen, Operando monitoring of temperature and active species at the single catalyst particle level. *Nat. Catal.* **2**, 986–996 (2019).
10. J. Stötzel, R. Frahm, B. Kimmerle, M. Nachtegaal, J.-D. Grunwaldt, Oscillatory behavior during the catalytic partial oxidation of methane: Following dynamic structural changes of palladium using the QEXAFS technique. *J. Phys. Chem. C* **116**, 599–609 (2012).
11. A. M. Gänzler, M. Casapu, A. Boubnov, O. Müller, S. Conrad, H. Lichtenberg, R. Frahm, J. D. Grunwaldt, *Operando* spatially and time-resolved X-ray absorption spectroscopy and infrared thermography during oscillatory CO oxidation. *J. Catal.* **328**, 216–224 (2015).
12. E. Gross, Uncovering the deactivation mechanism of Au catalyst with *operando* high spatial resolution IR and X-ray microspectroscopy measurements. *Surf. Sci.* **648**, 136–140 (2016).
13. A. T. Bell, The impact of nanoscience on heterogeneous catalysis. *Science* **299**, 1688–1691 (2003).
14. A. Tanimu, S. Jaenicke, K. Alhooshani, Heterogeneous catalysis in continuous flow microreactors: A review of methods and applications. *Chem. Eng. J.* **327**, 792–821 (2017).

15. B. A. Rizkin, F. G. Popovic, R. L. Hartman, Review Article: Spectroscopic microreactors for heterogeneous catalysis. *J. Vac. Sci. Technol. A* **37**, 050801 (2019).
16. P. C. K. Vesborg, J. L. Olsen, T. R. Henriksen, I. Chorkendorff, O. Hansen, Gas-phase photocatalysis in μ-reactors. *Chem. Eng. J.* **160**, 738–741 (2010).
17. T. R. Henriksen, J. L. Olsen, P. Vesborg, I. Chorkendorff, O. Hansen, Highly sensitive silicon microreactor for catalyst testing. *Rev. Sci. Instrum.* **80**, 124101 (2009).
18. S. Levin, J. Fritzsche, S. Nilsson, A. Runemark, B. Dhokale, H. Ström, H. Sundén, C. Langhammer, F. Westerlund, A nanofluidic device for parallel single nanoparticle catalysis in solution. *Nat. Commun.* **10**, 4426 (2019).
19. S. Alekseeva, A. B. da Silva Fanta, B. Iandolo, T. J. Antosiewicz, F. A. A. Nugroho, J. B. Wagner, A. Burrows, V. P. Zhdanov, C. Langhammer, Grain boundary mediated hydriding phase transformations in individual polycrystalline metal nanoparticles. *Nat. Commun.* **8**, 1084 (2017).
20. J. Fritzsche, D. Albinsson, M. Fritzsche, T. J. Antosiewicz, F. Westerlund, C. Langhammer, Single particle nanoplasmonic sensing in individual nanofluidic channels. *Nano Lett.* **16**, 7857–7864 (2016).
21. A. Beskok, G. E. Karniadakis, Report: A model for flows in channels, pipes, and ducts at micro and nano scales. *Microsc. Thermophys. Eng.* **3**, 43–77 (1999).
22. C. Langhammer, B. Kasemo, I. Zorić, Absorption and scattering of light by Pt, Pd, Ag, and Au nanodisks: absolute cross sections and branching ratios. *J. Chem. Phys.* **126**, 194702 (2007).
23. C. Langhammer, E. M. Larsson, B. Kasemo, I. Zorić, Indirect nanoplasmonic sensing: Ultrasensitive experimental platform for nanomaterials science and optical nanocalorimetry. *Nano Lett.* **10**, 3529–3538 (2010).
24. N. Liu, M. L. Tang, M. Hentschel, H. Giessen, A. P. Alivisatos, Nanoantenna-Enhanced Gas Sensing in a Single Tailored Nanofocus. *Nat. Mater.* **10**, 631–636 (2011).
25. T. Shegai, C. Langhammer, Hydride formation in single palladium and magnesium nanoparticles studied by nanoplasmonic dark-field scattering spectroscopy. *Adv. Mater.* **23**, 4409–4414 (2011).
26. S. Syrenova, C. Wadell, F. A. A. Nugroho, T. A. Gschneidtner, Y. A. Diaz Fernandez, G. Nalin, D. Świtlik, F. Westerlund, T. J. Antosiewicz, V. P. Zhdanov, K. Moth-Poulsen, C. Langhammer, Hydride formation thermodynamics and hysteresis in individual Pd nanocrystals with different size and shape. *Nat. Mater.* **14**, 1236–1244 (2015).
27. B. Hammer, J. K. Norskov, Why gold is the noblest of all the metals. *Nature* **376**, 238–240 (1995).
28. S. R. Chemler, Copper catalysis in organic synthesis. *Beilstein J. Org. Chem.* **11**, 2252–2253 (2015).
29. T. L. LeValley, A. R. Richard, M. Fan, The progress in water gas shift and steam reforming hydrogen production technologies – A review. *Int. J. Hydrogen Energy* **39**, 16983–17000 (2014).

30. C. Ratnasamy, J. P. Wagner, Water gas shift catalysis. *Catal. Rev.* **51**, 325–440 (2009).
31. Z. Zhang, S.-S. Wang, R. Song, T. Cao, L. Luo, X. Chen, Y. Gao, J. Lu, W.-X. Li, W. Huang, The most active Cu facet for low-temperature water gas shift reaction. *Nat. Commun.* **8**, 488 (2017).
32. Y. Bu, J. W. H. Niemantsverdriet, H. O. A. Fredriksson, Cu model catalyst dynamics and CO oxidation kinetics studied by simultaneous in situ UV–Vis and mass spectroscopy. *ACS Catal.* **6**, 2867–2876 (2016).
33. G. H. Chan, J. Zhao, E. M. Hicks, G. C. Schatz, R. P. Van Duyne, Plasmonic properties of copper nanoparticles fabricated by nanosphere lithography. *Nano Lett.* **7**, 1947–1952 (2007).
34. S. Nilsson, D. Albinsson, T. J. Antosiewicz, J. Fritzsche, C. Langhammer, Resolving single Cu nanoparticle oxidation and Kirkendall void formation with in situ plasmonic nanospectroscopy and electrodynamic simulations. *Nanoscale* **11**, 20725–20733 (2019).
35. H. Falsig, B. Hvolbæk, I. S. Kristensen, T. Jiang, T. Bligaard, C. H. Christensen, J. K. Nørskov, Trends in the catalytic CO oxidation activity of nanoparticles. *Angew. Chem. Int. Ed.* **47**, 4835–4839 (2008).
36. B. Eren, C. Heine, H. Bluhm, G. A. Somorjai, M. Salmeron, Catalyst Chemical State during CO Oxidation Reaction on Cu(111) Studied with Ambient-Pressure X-ray Photoelectron Spectroscopy and Near Edge X-ray Adsorption Fine Structure Spectroscopy. *J. Am. Chem. Soc.* **137**, 11186–11190 (2015).
37. G. G. Jernigan, G. A. Somorjai, Carbon monoxide oxidation over three different oxidation states of copper: Metallic copper, copper (I) oxide, and copper (II) oxide - a surface science and kinetic study. *J. Catal.* **147**, 567–577 (1994).
38. F. Xu, K. Mudiyanselage, A. E. Baber, M. Soldemo, J. Weissenrieder, M. G. White, D. J. Stacchiola, Redox-mediated reconstruction of copper during carbon monoxide oxidation. *J. Phys. Chem. C* **118**, 15902–15909 (2014).
39. T.-J. Huang, D.-H. Tsai, CO oxidation behavior of copper and copper oxides. *Catal. Lett.* **87**, 173–178 (2003).
40. E. D. Palik, *Handbook of Optical Constants of Solids* (Academic Press, 1998), vol. 2, 1096pp.
41. H. J. Hagemann, W. Gudat, C. Kunz, Optical constants from the far infrared to the x-ray region: Mg, Al, Cu, Ag, Au, Bi, C, and $Al_2O_3$. *J. Opt. Soc. Am.* **65**, 742–744 (1975).
42. D. Tahir, S. Tougaard, Electronic and optical properties of Cu, CuO and $Cu_2O$ studied by electron spectroscopy. *J. Phys. Condens. Matter* **24**, 175002 (2012).
43. S. Alekseeva, I. I. Nedrygailov, C. Langhammer, Single particle plasmonics for materials science and single particle catalysis. *ACS Photonics* **6**, 1319–1330 (2019).

44. F. D. Manchester, A. San-Martin, J. M. Pitre, The H-Pd (hydrogen-palladium) system. *J. Phase Equilib.* **15**, 62–83 (1994).
45. R. J. Behm, V. Penka, M. G. Cattania, K. Christmann, G. Ertl, Evidence for "subsurface" hydrogen on Pd(110): An intermediate between chemisorbed and dissolved species. *J. Chem. Phys.* **78**, 7486–7490 (1983).
46. H. Fredriksson, Y. Alaverdyan, A. Dmitriev, C. Langhammer, D. S. Sutherland, M. Zäch, B. Kasemo, Hole-mask colloidal lithography. *Adv. Mater.* **19**, 4297–4302 (2007).
47. X. He, Y. Wang, X. Zhang, M. Dong, G. Wang, B. Zhang, Y. Niu, S. Yao, X. He, H. Liu, Controllable in situ surface restructuring of cu catalysts and remarkable enhancement of their catalytic activity. *ACS Catal.* **9**, 2213–2221 (2019).